Supplement of Nat. Hazards Earth Syst. Sci., 26, 3741–3748, 2026
https://doi.org/10.5194/nhess-26-3741-2026-supplement

Natural Hazards and Earth System Sciences
Open Access

Supplement of

Brief communication: Atmospheric moisture and near-surface temperature anomalies: key drivers in the 2022 European mega-drought

José C. Fernández-Alvarez et al.

Correspondence to: José C. Fernández-Alvarez (jcfernandez@cesga.es)

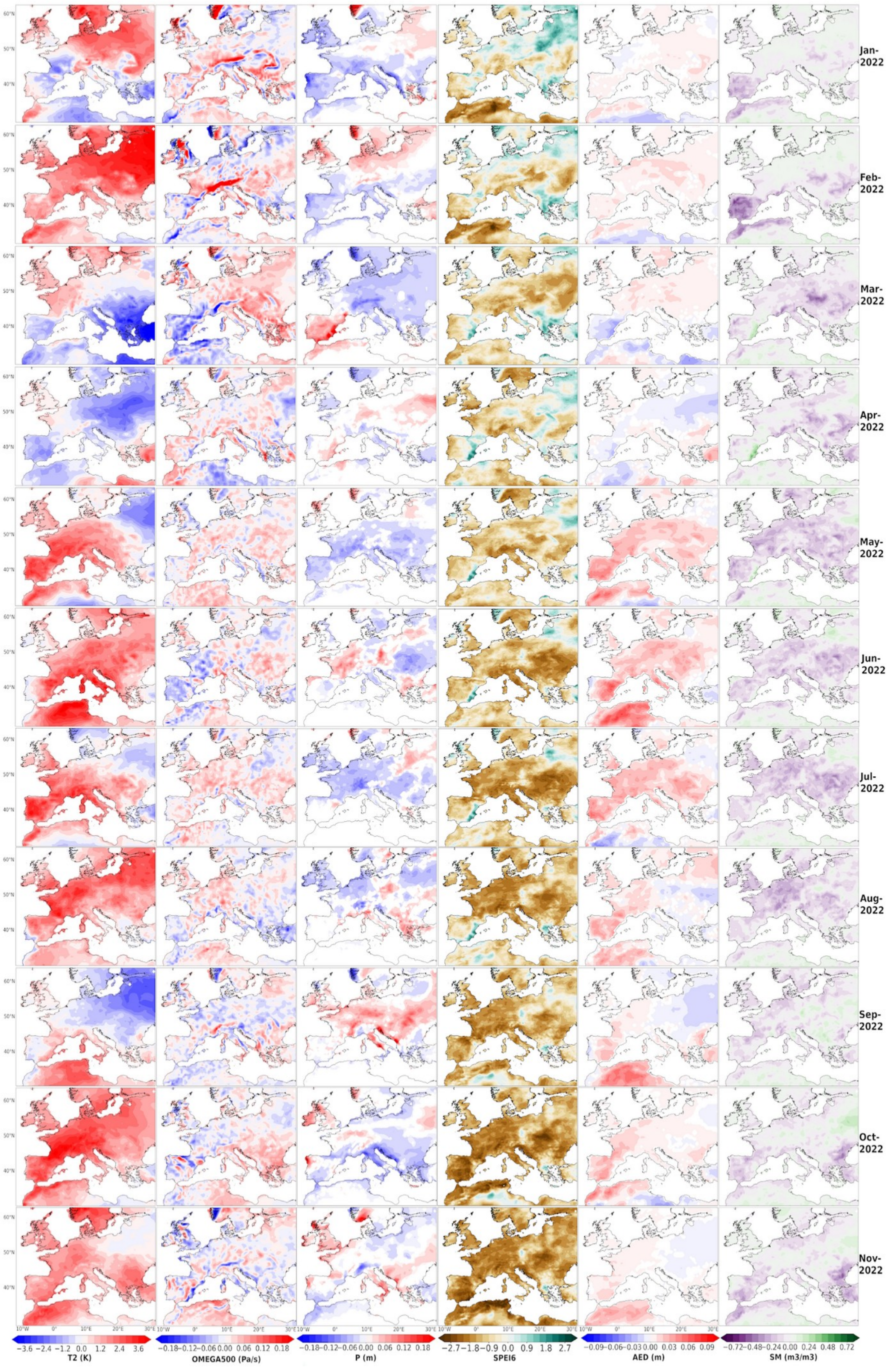

Figure S1. Monthly spatial evolution of meteorological anomalies | The figure shows the analysed meteorological variables from January to November 2022 (rows). The columns represent the following variables in order: air temperature at 2 m (T2, K), vertical velocity at 500 hPa (omega500, Pa s^{-1}), monthly accumulated precipitation (P, m), 6-month Standardized Precipitation Evapotranspiration Index (SPEI6), atmospheric evaporative demand (AED, m), and soil moisture (SM, m^3 m^{-3}). The analysis covers the period from 1994 to 2023. Data from the ERA5 reanalysis.

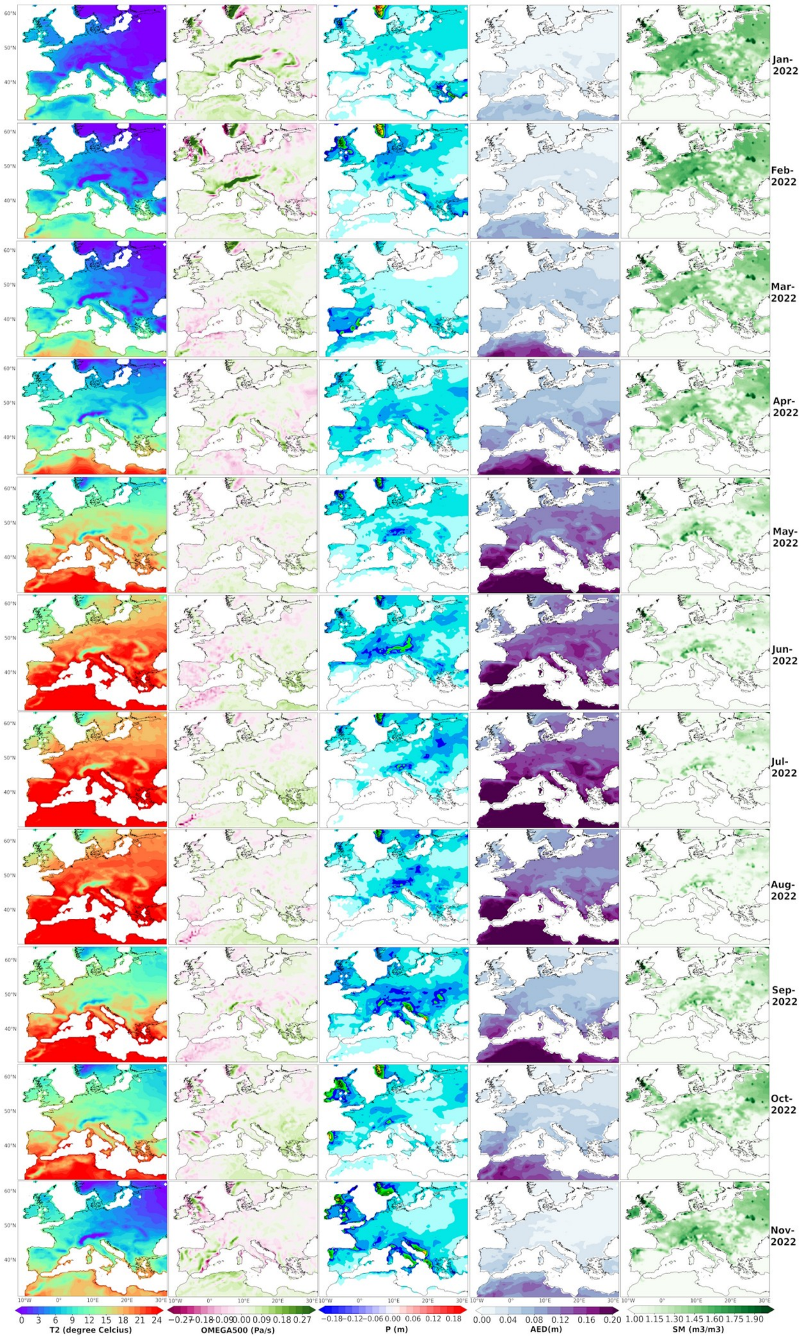

Figure S2. Monthly spatial evolution of meteorological variables | The figure presents the various meteorological variables analysed from January to November 2022 (top to bottom). The columns represent the following variables in order: air temperature at 2 m (T2, °C), vertical velocity at 500 hPa (omega500, Pa s^{-1}), monthly accumulated precipitation (P, m), 6-month Standardized Precipitation Evapotranspiration Index (SPEI6), atmospheric evaporative demand (AED, m), and soil moisture (SM, m^3 m^{-3}). The analysis covers the period from 1994 to 2023. Data from the ERA5 reanalysis.

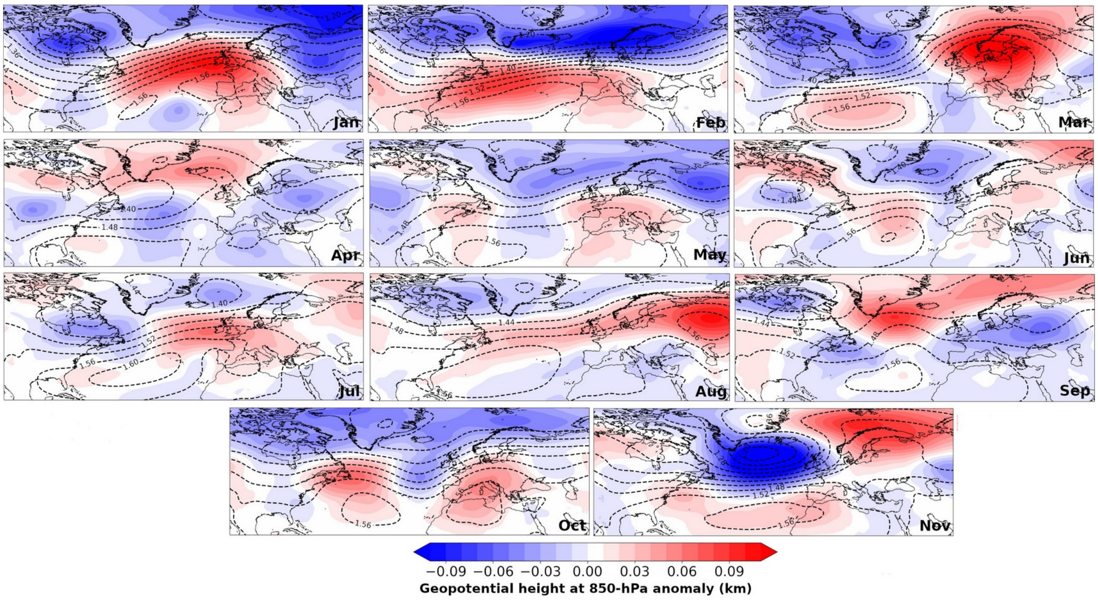

Figure S3. The geopotential height at 850 hPa (Z850) monthly anomaly and its absolute field for the North Atlantic region and Europe | The figure presents the monthly anomaly of Z850 (km, coloured filled) and the Z850 module (km, black contours) from January to November 2022 (top to bottom). The analysis covers the period from 1994 to 2023. Data from the ERA5 reanalysis.

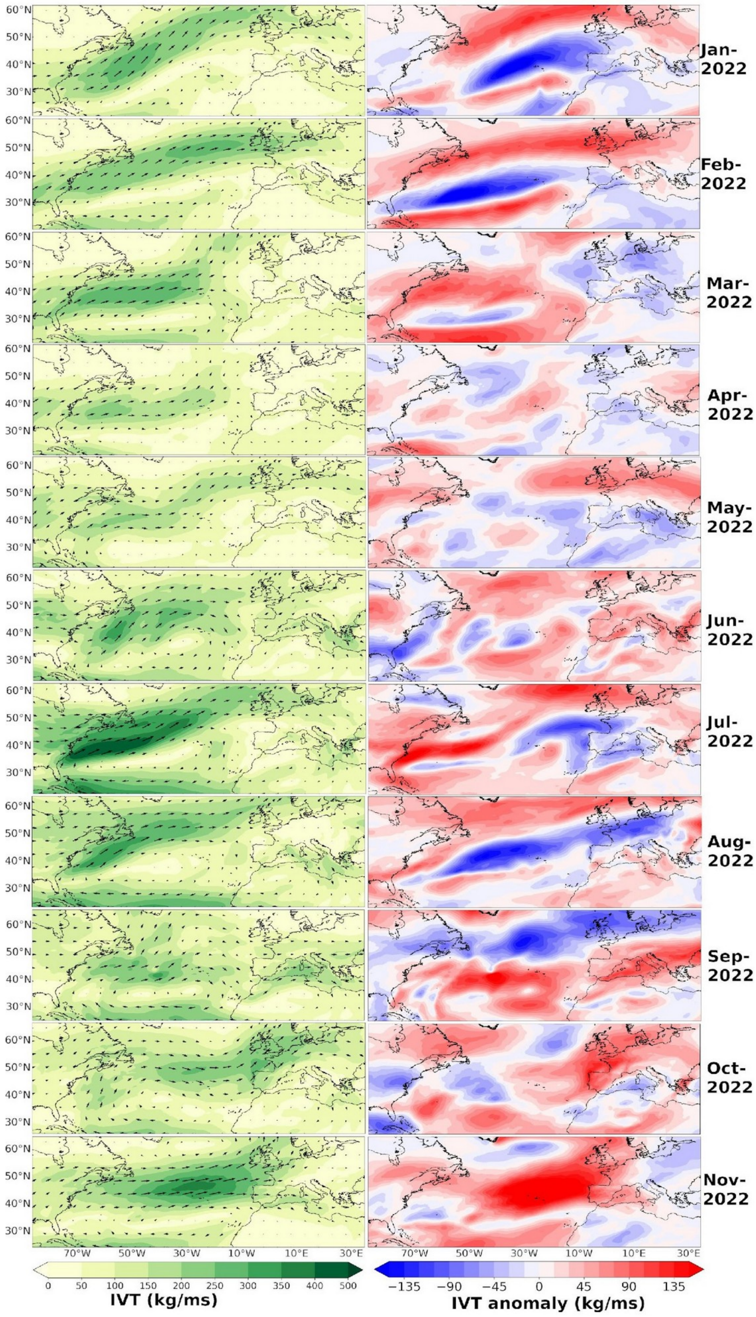

Figure S4. The vertically integrated water vapour transport (IVT) and its monthly anomaly for the North Atlantic region and Europe | The figure presents the IVT (kg m^{-1} s^{-1}) module (coloured filled, first column) and direction (arrows) and its monthly anomaly (kg m^{-1} s^{-1}, second column) from January to November 2022 (top to bottom). The analysis covers the period from 1994 to 2023. Data from the ERA5 reanalysis.

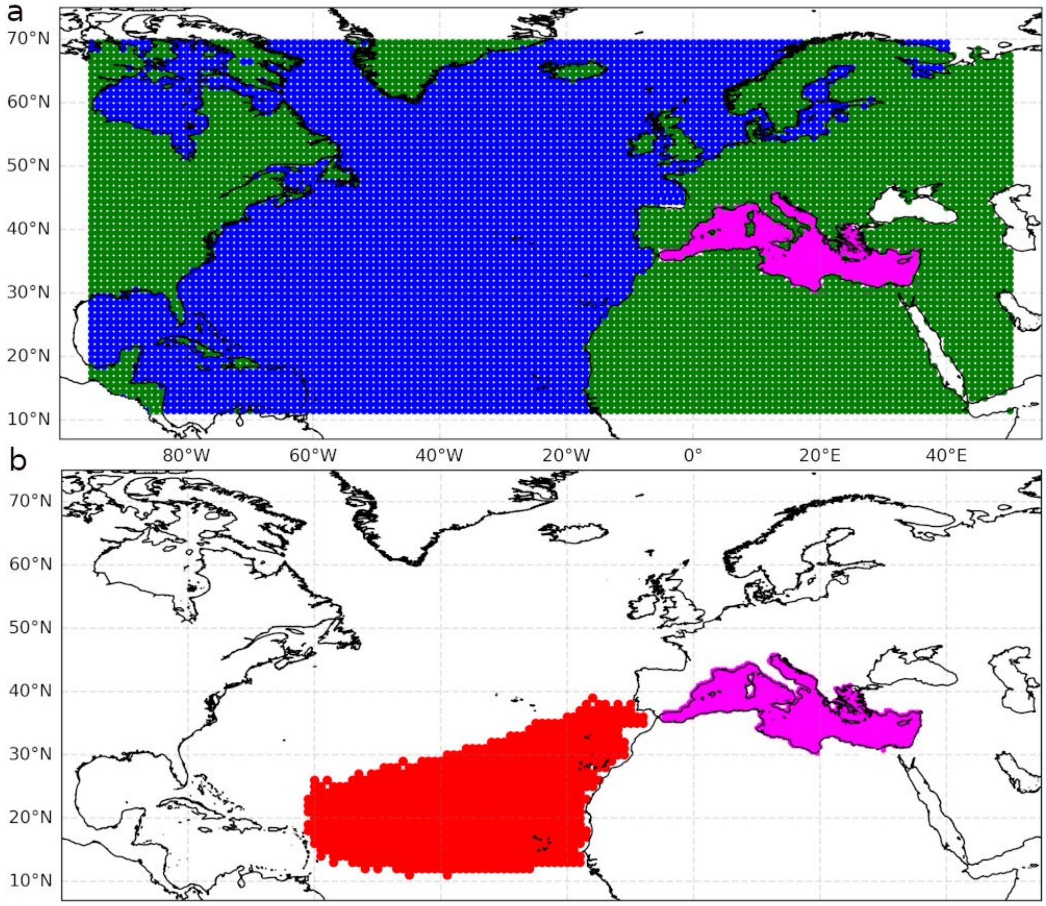

Figure S5. Spatial domains and masks used in this study I a) Masks defined for the moisture uptake (MU) and temperature anomaly analyses within the North Atlantic domain, comprising the general land sector (green), the ocean sector (blue), and the Mediterranean Sea (MED, magenta). Note that when evaluating a specific European target subregion (NE_Europe or NW_Europe; see Fig. 1a), that subregion is dynamically excluded from the general green land sector to guarantee non-overlapping domains. b) Masks defined for the Precipitation Contribution (PC) analysis, including the North Atlantic Ocean source region (NATL, red), the Mediterranean Sea source region (MED, magenta), and the two target European subregions (NE_Europe and NW_Europe; see Fig. 1a). All masks are mutually exclusive to prevent spatial overlap.

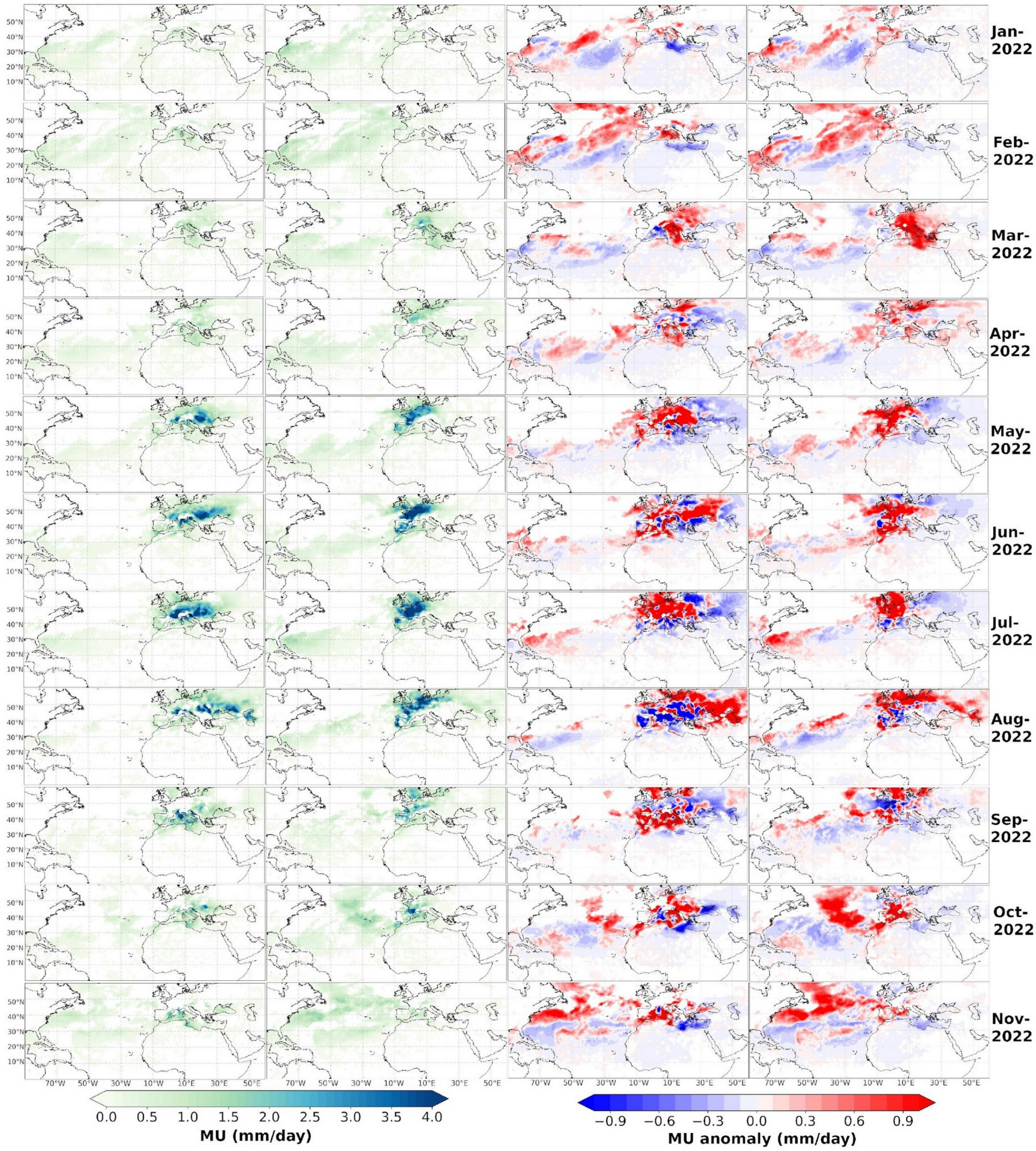

Figure S6. Monthly spatial evolution of moisture uptake (MU) pattern | The figure shows the spatial patterns of moisture uptake (mm day^{-1}) and its anomalies (mm day^{-1}) from January to November 2022 (top to bottom). The first and third columns correspond to SE_Europe, while the second and fourth columns represent NW_Europe. The analysis period spans from 1994 to 2023. Processed data from FLEXPART outputs using TROVA software.

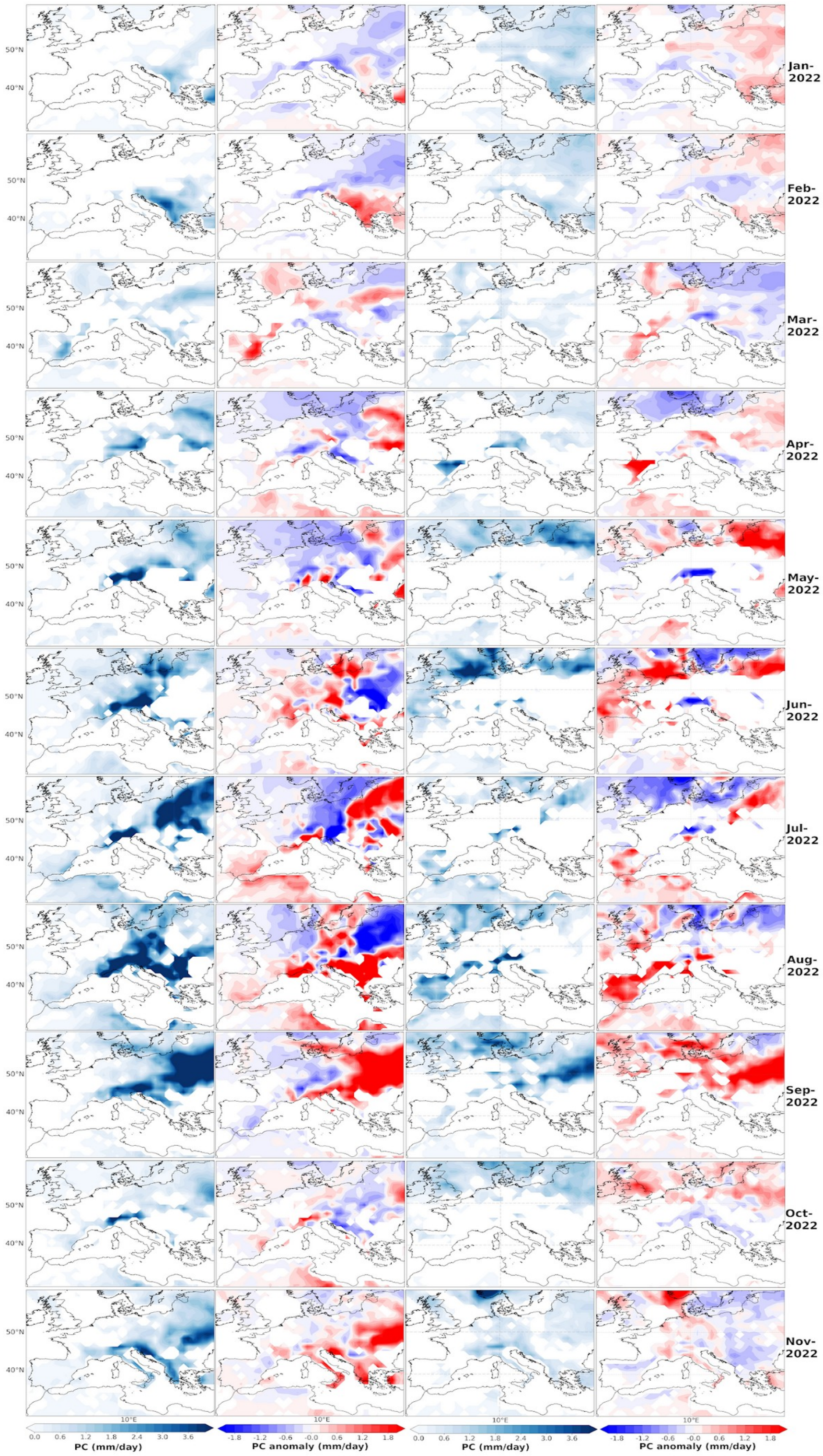

Figure S7. Moisture sink patterns (precipitation contributions, PCs) associated with target regions and their monthly anomalies | The first to second columns correspond to SE_Europe and the third to fourth columns correspond to NW_Europe. From top to bottom the months from January to November 2022. The pattern of moisture sinks (P-E >0) and anomalies are represented in mm day^{-1}. The analysis covers the period from 1994 to 2023. Processed data from FLEXPART outputs using TROVA software.

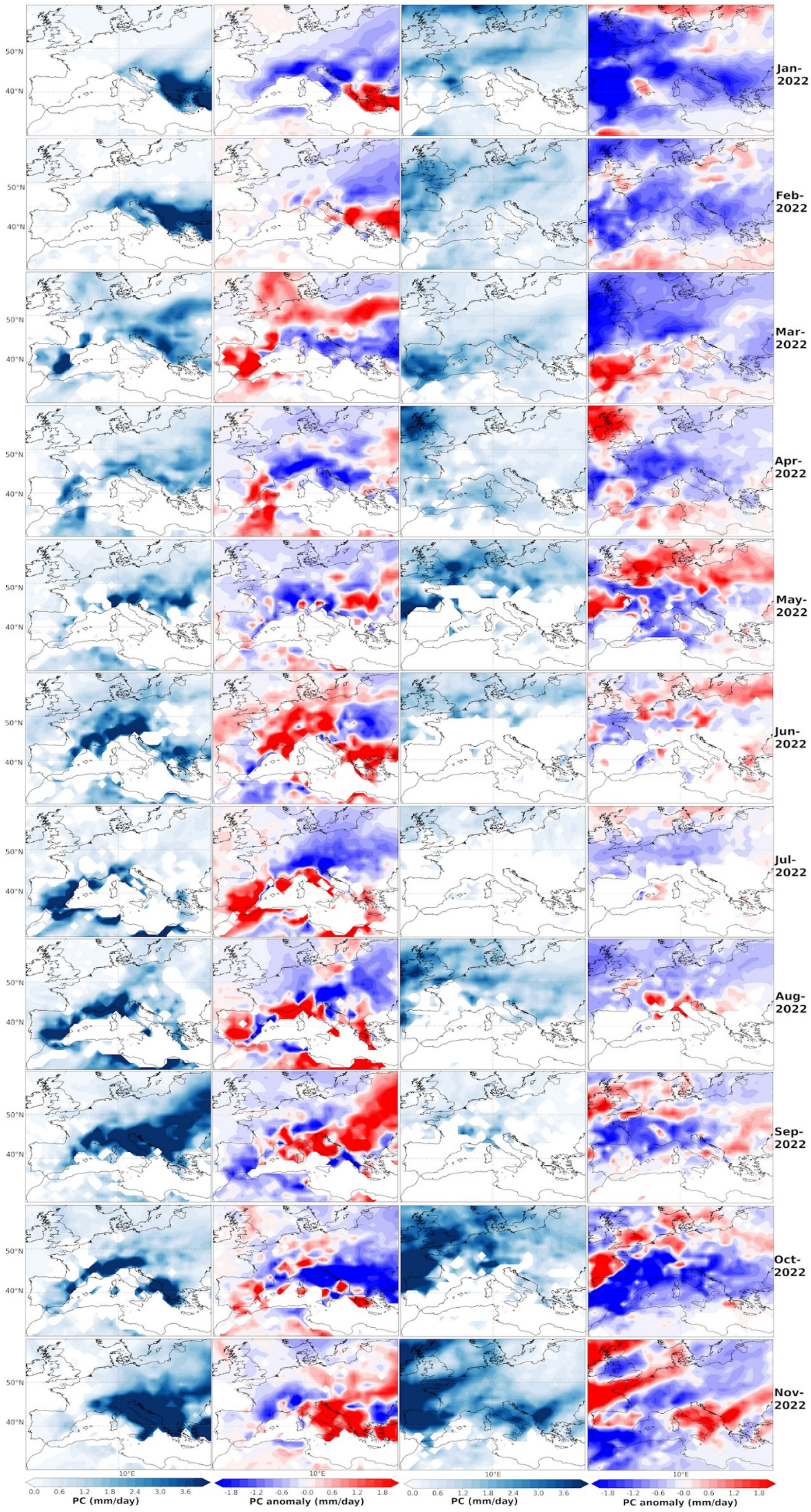

Figure S8. Moisture sink patterns (precipitation contributions, PCs) associated with different moisture sources and their monthly anomalies | The first to second columns correspond to the Mediterranean Sea source (MED) and the third to fourth columns correspond to the North Atlantic Ocean source (NATL). From top to bottom, the months from January to November 2022. The pattern of moisture sinks (P-E >0) and its anomaly are represented in mm day^{-1}. The analysis covers the period from 1994 to 2023. Processed data from FLEXPART outputs using TROVA software.

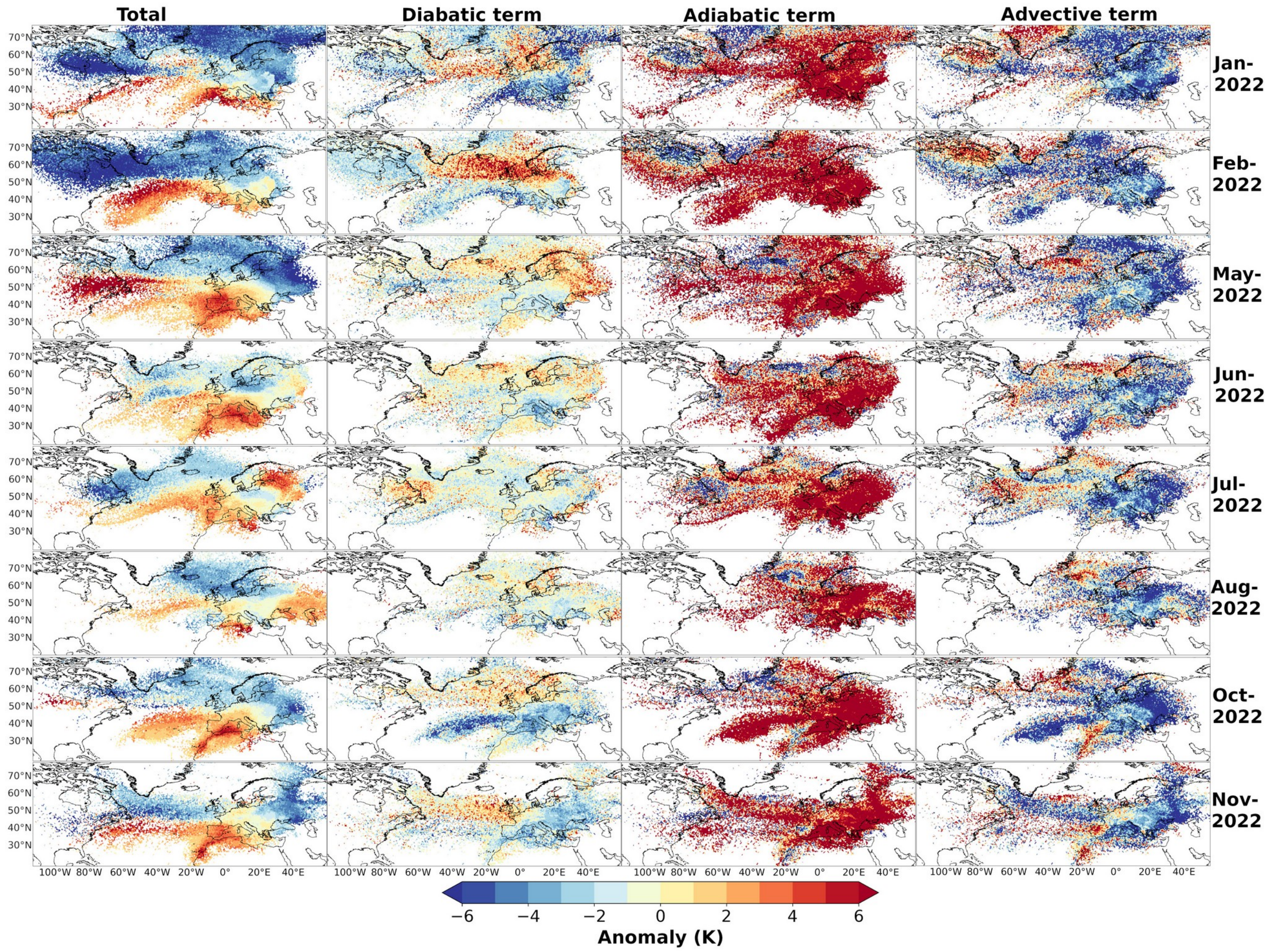

Figure S9. Spatial pattern of temperature anomaly sources related to the 2022 European drought using SE_Europe as target region | The columns (left to right) show temperature anomalies (K) for the months in 2022 with positive anomalies (January, February, May, June, July, August, October, and November). The first column represents the total anomaly (T′), while the following columns correspond to diabatic (T_{diab}), adiabatic (T_{adiab}) and advective (T_{adv}) components. The analysis covers the period from 1994 to 2023. Processed data from FLEXPART outputs.

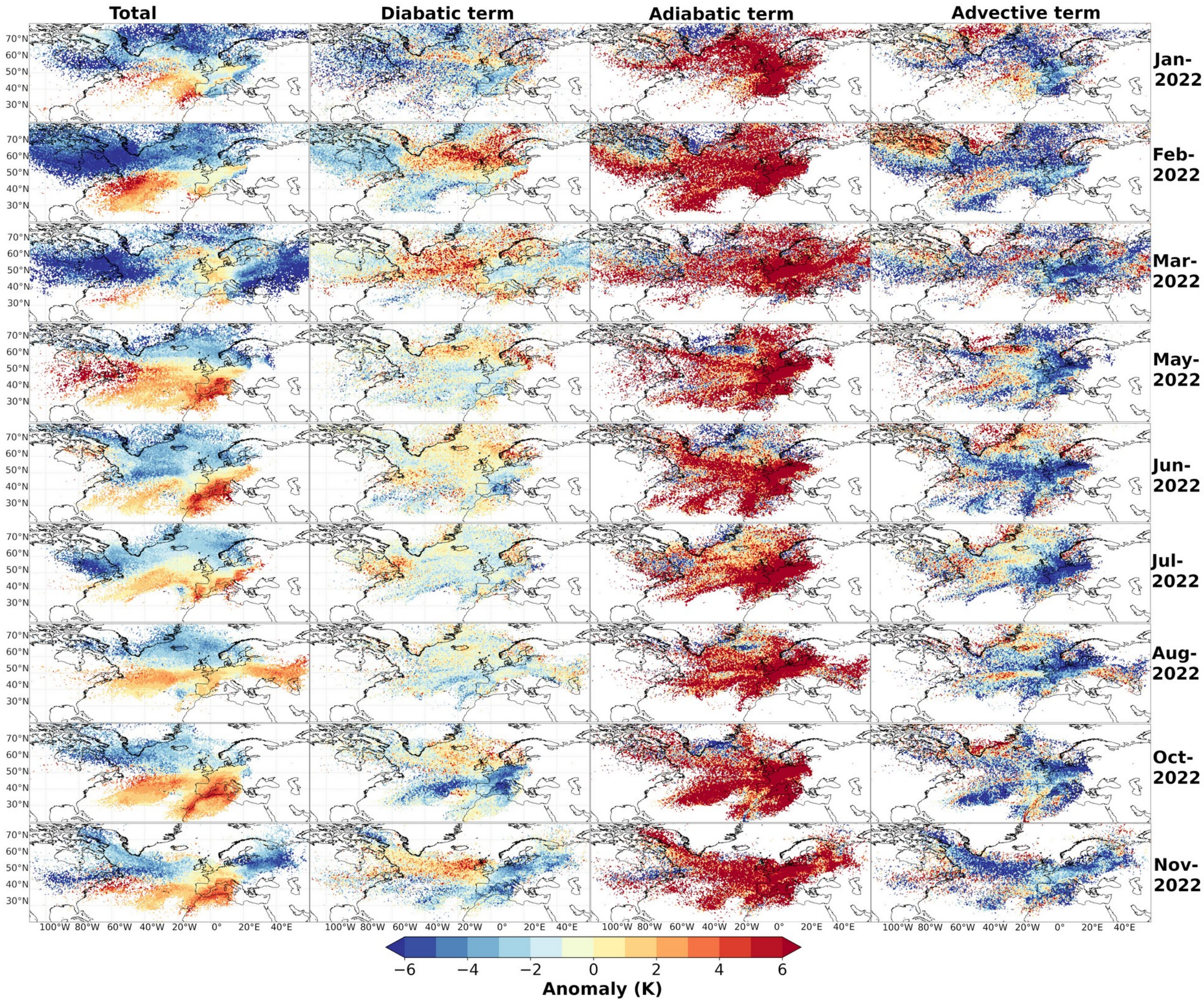

Figure S10. Spatial pattern of temperature anomaly sources related to the 2022 European drought using NW_Europe as target region | The columns (left to right) show temperature anomalies (K) for the months in 2022 with positive anomalies (January, February, May, June, July, August, October, and November). The first column represents the total anomaly (T′), while the following columns correspond to diabatic (T_{diab}), adiabatic (T_{adiab}) and advective (T_{adv}) components. The analysis covers the period from 1994 to 2023. Processed data from FLEXPART outputs.

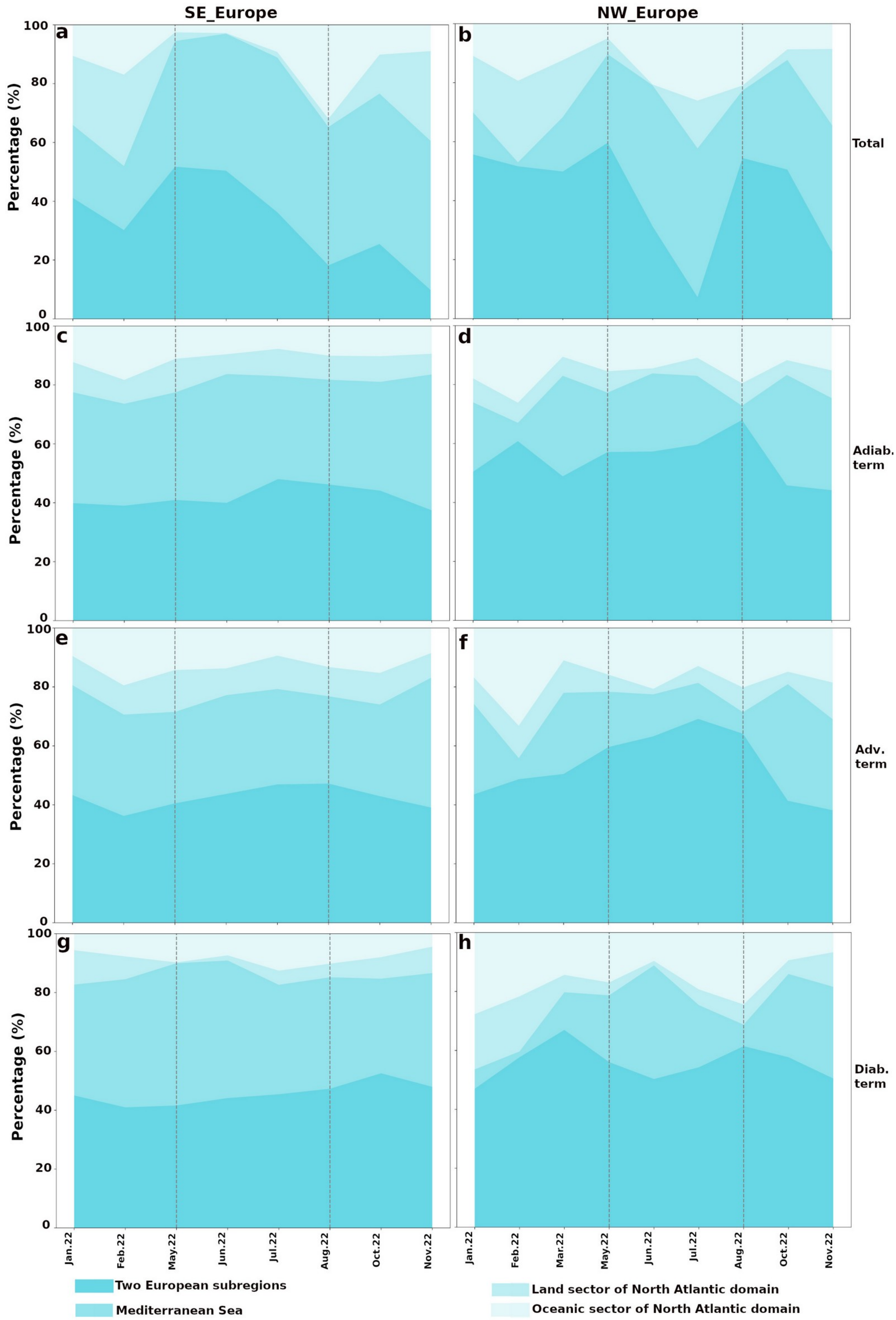

Figure S11. Percentage contributions of regional source areas to monthly temperature anomalies for SE_Europe and NW_Europe during the 2022 European drought | Stacked area plots show the relative influence of four source regions—the two European subregions, the Mediterranean Sea, and the land and ocean sectors of the North Atlantic domain—on the total (a,b), adiabatic (c, d), advective (e, f), and diabatic (g, h) temperature anomalies. The framed perriod highlights the active hydro-climatic drought peak period (May–August 2022). The analysis covers the period from 1994 to 2023. Processed data from FLEXPART outputs.

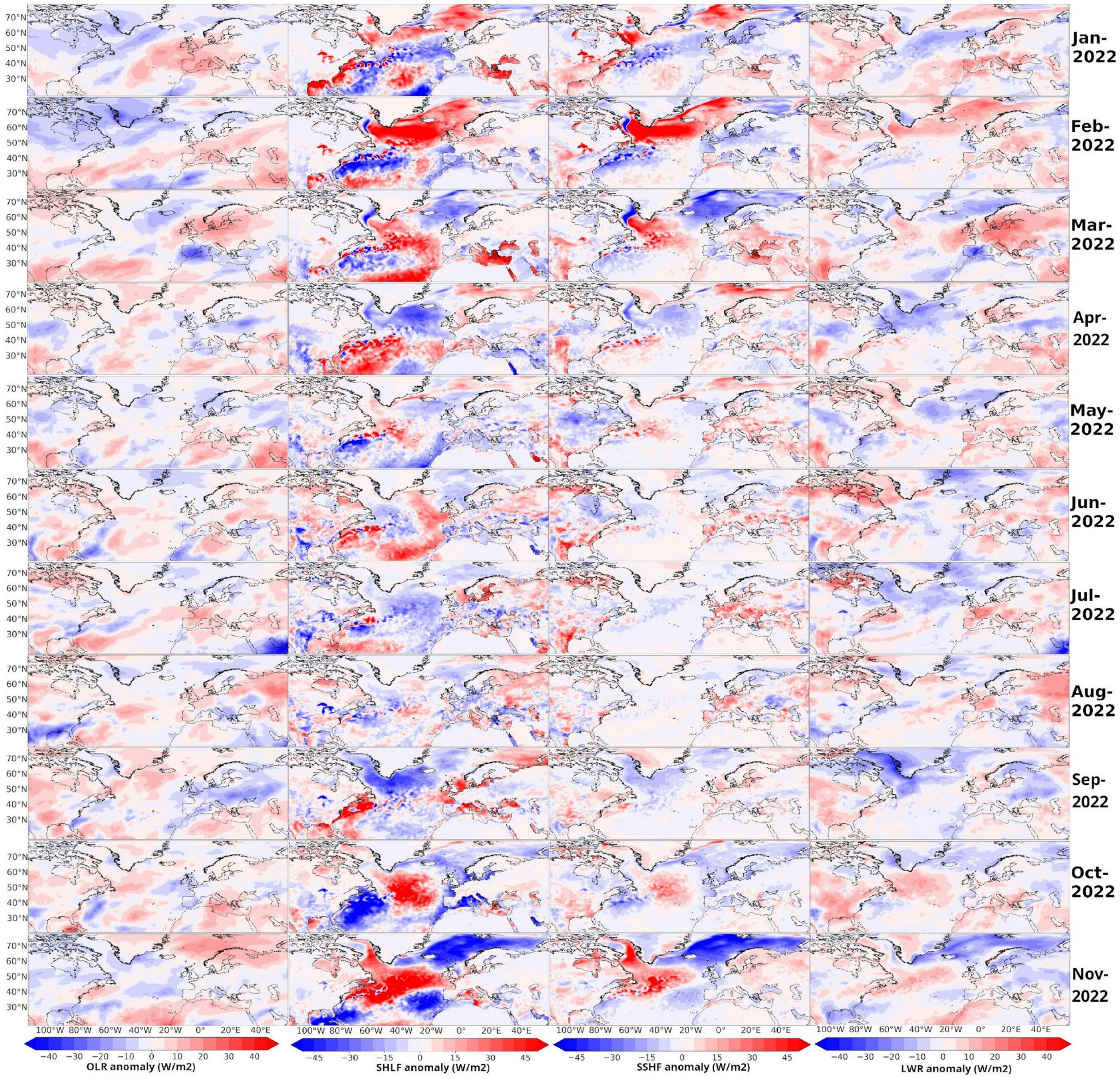

Figure S12. Monthly anomalies of surface fluxes and radiation for the North Atlantic region and Europe during the 2022 European drought | Spatial distribution of monthly anomalies in outgoing longwave radiation (OLR, W m^{-2}, first column), surface latent heat flux (SLHF, W m^{-2}, second column), surface sensible heat flux (SSHF, W m^{-2}, third column), and net longwave radiation (LWR, W m^{-2}, fourth column) from January to November 2022. Red (blue) shading indicates positive (negative) departures from the climatological mean. The analysis covers the period from 1994 to 2023. Data from the ERA5 reanalysis.

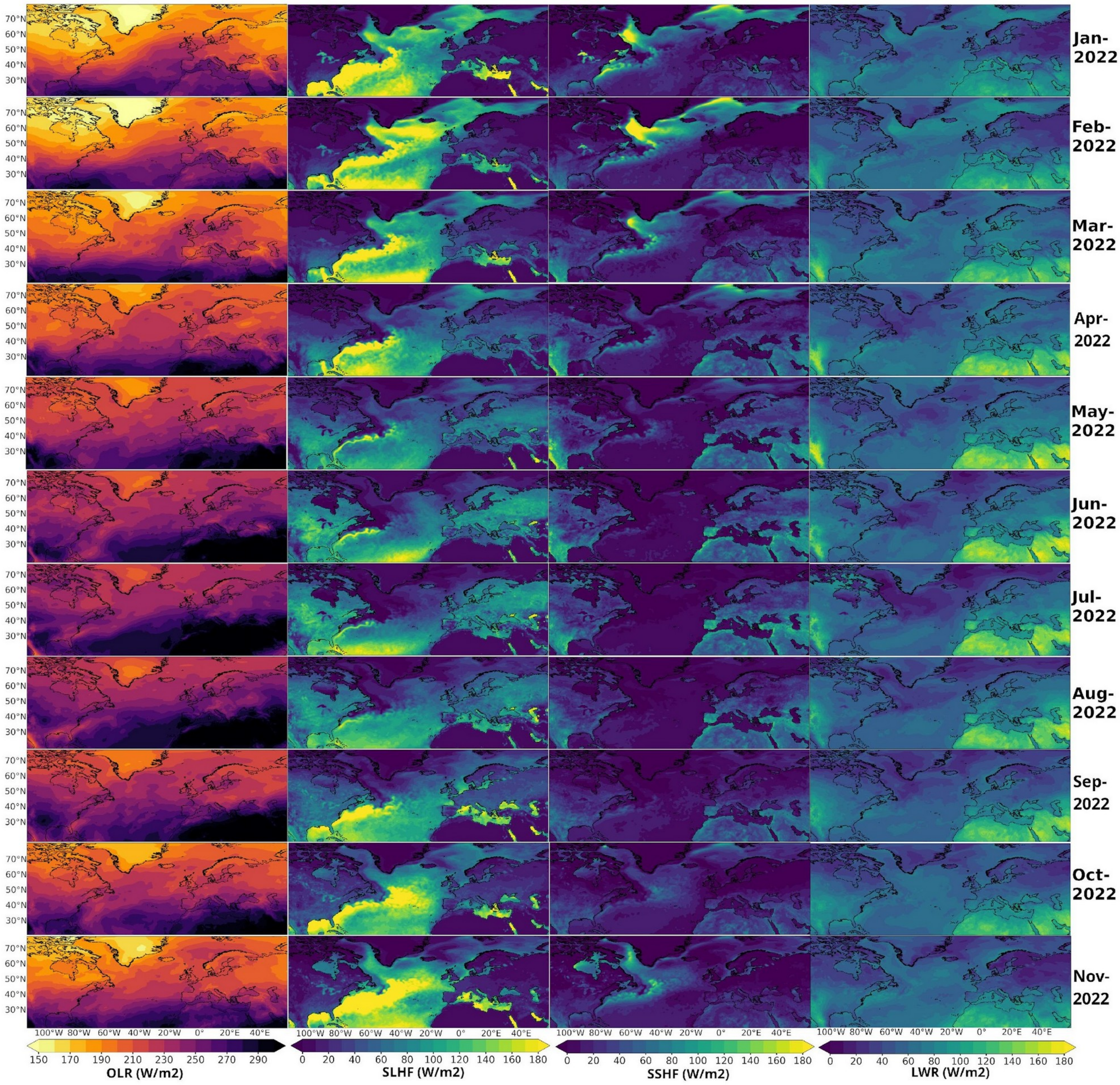

Figure S13. Monthly patterns of surface fluxes and radiation for the North Atlantic region and Europe during the 2022 European drought | Spatial distribution of monthly patterns in outgoing longwave radiation (OLR, W m^{-2}, first column), surface latent heat flux (SLHF, W m^{-2}, second column), surface sensible heat flux (SSHF, W m^{-2}, third column), and net longwave radiation (LWR, W m^{-2}, fourth column) from January to November 2022. The analysis covers the period from 1994 to 2023. Data from the ERA5 reanalysis.

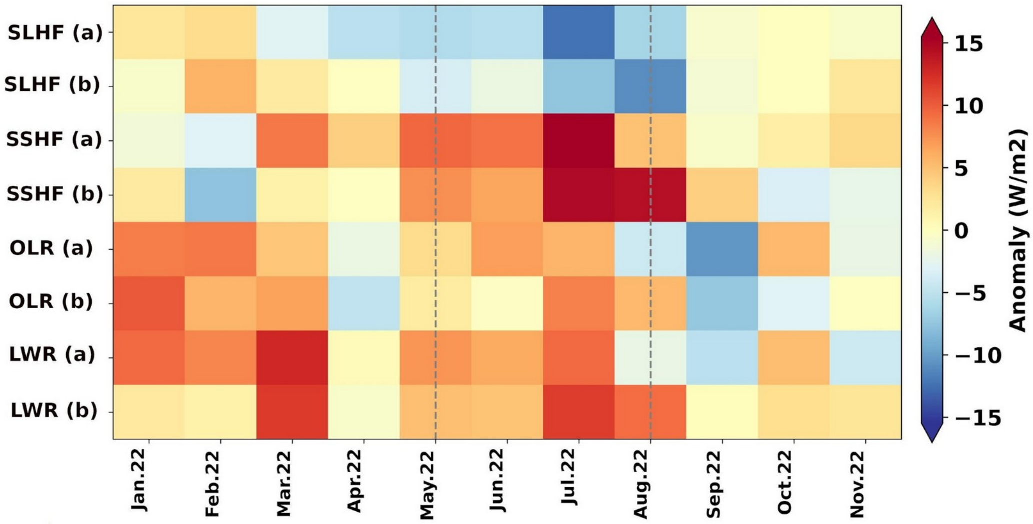

Figure S14. Monthly anomalies of surface fluxes and radiation in SE_Europe (a) and NW_Europe (b) during the 2022 European drought | Heat map of monthly anomalies for surface latent heat flux (SLHF, W m^{-2}), surface sensible heat flux (SSHF, W m^{-2}), outgoing longwave radiation (OLR, W m^{-2}), and net longwave radiation (LWR, W m^{-2}) averaged over the SE_Europe and NW_Europe domains from January to November 2022. Positive (negative) anomalies are shown in red (blue). The framed period highlights the active hydro-climatic drought peak period (May–August 2022). The analysis covers the period from 1994 to 2023. Data from the ERA5 reanalysis.

Supplementary Methods

Data employed

Moisture and temperature Lagrangian analysis in this study are based on data outputs from the global particle dispersion model FLEXPARTv10.4 [2], forced with ERA5 reanalysis data [3]. ERA5 provides 3-hourly fields at 0.5° horizontal resolution and 137 vertical levels from the surface to 1 hPa. FLEXPART simulations tracked the dispersion of 30 million particles globally [4].

ERA5 data (1994–2023) were also used to compute anomalies of meteorological variables for January–November 2022 at 0.5° spatial resolution. Variables include vertical velocity at 500 hPa (omega500, Pa s^{-1}), 2 m air temperature (T2, K), total precipitation (P, m), vertically integrated water vapour transport (IVT, kg m^{-1} s^{-1}), atmospheric evaporative demand (AED, m), soil moisture (SM, m^3 m^{-3}), geopotential height at 850 hPa (Z850, km), surface latent heat flux (SLHF, W m^{-2}), surface sensible heat flux (SSHF, W m^{-2}), surface net long-wave (thermal) radiation (LWR, W m^{-2}) and outgoing long-wave radiation (OLR, W m^{-2}). Vertical pressure and air temperature at model levels were considered for tracking the sources of temperature anomalies (see section below).

Additionally, ERALand data at 0.1° resolution over the Euro-Mediterranean domain (15°W–32°E, 30°N–62°N) were used to calculate SPEI with reference period 1965–2022. Monthly averages of precipitation, maximum and minimum air temperature, relative humidity, solar radiation, wind speed, surface run-off, and total soil moisture were considered [5].

Identifying the target regions for Lagrangian tracking analysis

The drought-affected area in Europe was defined using the 6-month Standardized Precipitation Evapotranspiration Index (SPEI6) [6] from ERA5-Land data [7]. Necessary AED values were inferred from the FAO-56 Penman-Monteith equation [8]. Regions with SPEI6 ≤ –1.28, corresponding to moderate drought conditions (return period ≈ 10 years) [9], were selected. The final study region represents the combined area affected during June–August (JJA) 2022 (Fig. 1a in Manuscript), capturing the core phase of compound summer heat and drought, consistent with previous assessments of the 2021–2022 Euro-Mediterranean drought [7].

Crucially, this summer window (JJA) encapsulates the maximum atmospheric evaporative demand driven by record-breaking temperature anomalies and persistent heatwaves—key drivers for our atmospheric and Lagrangian temperature anomaly analysis. While multi-scalar indices like SPEI6 inherently exhibit minimum values later in autumn due to the cumulative 6-month memory effect of preceding moisture deficits (Fig. 1c in Manuscript), those later periods coincide with weaker thermal stress, increased synoptic instability, and the onset of hydrological recovery (Fig. 2 in Manuscript). Using June–August therefore ensures that the study mask targets the peak compound heat–drought conditions, avoiding contamination from the drought-breaking phase.

As demonstrated by Gimeno-Sotelo et al. [10], droughts in northwestern Europe are primarily driven by North Atlantic Ocean moisture deficits, while central and eastern Europe are mainly affected by Mediterranean deficits. Accordingly, the 2022 European drought area was divided into two areas of influence—NW_Europe and SE_Europe (Fig. 1a in Manuscript)— for tracking moisture transport and temperature anomalies.

Lagrangian approach for the moisture source and sink patterns

To estimate moisture sources and sinks, a Lagrangian methodology tracked temporal changes in specific moisture content (q) along 30 million atmospheric particle trajectories (see Data Employed), and particle properties were recorded every 6 hours. Following Stohl and James [11], the rate of q change for each particle is:

$$(e-p)=m\left(\frac{dq}{dt}\right), \qquad \text{(S1)}$$

where m is particle mass, and $(e-p)$ accounts for the increase or decrease in the water vapour ratio along its trajectory. Total surface freshwater flux per grid cell was obtained by summing all particles' contributions through a grid A at a given time:

$$(E-P)=\frac{\sum_{k=1}^{N}(e-p)_k}{A}, \qquad \text{(S2)}$$

where E represents evaporation, P precipitation, and N the total number of particles over the grid cell. Particle trajectories were followed for 10 days, the average atmospheric residence time of water vapour [12]. The resulting E–P fields therefore represent integrated freshwater fluxes along this period.

Atmospheric particles can be tracked along their trajectories backward or forward in time from a target region to determine their moisture sources or sinks, respectively [11]. Backward-tracking identifies moisture sources (E–P > 0; areas where evaporation exceeds precipitation), indicating net moisture uptake (MU) by air parcels. This framework provides a comprehensive perspective on the origins of the moisture reaching drought-affected Europe by evaluating MU anomalies. To this end, MU anomalies were averaged over five predefined domains (Fig. S5a): the two European subregions affected by the drought (NE_Europe and NW_Europe, Fig. 1a in the Manuscript), the Mediterranean Sea (MED), the broader North Atlantic ocean sector, and the remaining continental North Atlantic land area (excluding the evaluated European subregion). Quantifying MU was crucial for assessing the contributions from each source and capturing the key components of the moisture transport dynamics that shape the drought conditions.

Forward-tracking identifies moisture sinks (E–P < 0; precipitation exceeds evaporation), representing areas where net moisture loss occurs. Forward simulations were conducted to quantify the moisture contributions for precipitation (PC) from Europe's main known sources—the Mediterranean (MED) and North Atlantic (NATL), defined in Gimeno et al. [13] and corroborated by Gimeno-Sotelo et al. [10] —as well as from the two drought-affected subregions (Fig. S5b).

Post-processing of E–P fields was carried out using TROVA software [14, 15].

Lagrangian approach for the temperature anomaly source patterns

To identify sources of temperature anomalies, we applied the Lagrangian framework by Papritz and Röthlisberger [16]. The study focused on months exhibiting positive near-surface temperature anomalies (Fig. 1h in Manuscript).

Lagrangian temperature anomalies (T') were defined as deviations of the temperature (T) from the model-based climatology $\overline{T}$, which accounts for daily and seasonal cycles. To calculate $\overline{T}$, for each specific date and time of the year, temperature values were averaged across all time steps from 1994 to 2023 within a ± 21-day window centred on the target date. Backward FLEXPART trajectories calculated every 6 hours traced T' sources up to 10 days backward in time. Only trajectories below 120 m altitude (near-surface level) at 00 UTC each day (initial time over the target region) were considered.

Variation in T' along the particle trajectory between the positions x_g at time t_g and x at time t is defined as follows [16]:

$$T'(x,t) - T'(x_g,t_g) = -\int_{t_g^{sea}}^{t} \frac{\partial \overline{T}}{\partial t} d\tau - \int_{t_g^{adv}}^{t} v * \nabla_h(\overline{T}) d\tau + \int_{t_g^{adi}}^{t} \left[\frac{\kappa T}{p} - \frac{\partial \overline{T}}{\partial p} \right] \omega d\tau + \int_{t_g^{dia}}^{t} \left(\frac{p}{p_0} \right)^{\kappa} \frac{D\theta}{Dt} d\tau \qquad \text{(S3)}$$

where v and ω are the horizontal and vertical wind components; $\overline{T}$ is temperature climatology; ∇_h is the horizontal gradient; κ is the Poisson constant; p_0 is 1000 hPa; and θ is potential temperature. Fields (i.e $\overline{T}$, θ, $\frac{\partial \overline{T}}{\partial p}$, $\frac{\partial \overline{T}}{\partial t}$) to T' decomposition were interpolated to particle positions, and resulting quantities were evaluated following Papritz and Röthlisberger [16]. The terms, from left to right, represent T' changes due to climatological variations (seasonality), horizontal advection, adiabatic processes, and diabatic heating/cooling. The seasonal term is not analysed as negligible. Finally, the relative contributions of these physical drivers were spatially integrated across the predefined land, ocean, and target subregion sectors (Fig. S5a).

References

[1] Fernández-Alvarez et al. (2023) Projected changes in atmospheric moisture transport contributions associated with climate warming in the North Atlantic, Nat. Comm., 14, 6476 ; DOI: 10.1038/s41467-023-41915-1.

[2] Pisso, I., et al. The Lagrangian particle dispersion model FLEXPART version 10.4. Geosci. Model Dev. 12, 4955–4997 (2019).

[3] Hersbach, H., Bell, B., Berrisford, P., Hirahara, S., Horányi, A., Muñoz-Sabater, J., et al. The ERA5 global reanalysis. Q. J. R. Meteorol. Soc., 146, 1999–2049 (2020).

[4] Vázquez, M., Alvarez-Socorro, G., Fernández-Alvarez, J. C., Nieto, R., & Gimeno, L. Global FLEXPART-ERA5 simulations using 30 million atmospheric parcels since 1980. Zenodo. https://doi.org/10.5281/zenodo.12204017 (2024).

[5] Muñoz-Sabater, J., et al. ERA5-Land: A state-of-the-art global reanalysis dataset for land applications. ESSD 13, 4349-4383 (2021).

[6] Vicente-Serrano, S. M., Beguería, S., López-Moreno, J. I. A multiscalar drought index sensitive to global warming: the standardized precipitation evapotranspiration index. J. Clim. 23(7), 1696-1718 (2010).

[7] Garrido-Pérez, J. M., Vicente-Serrano, S. M., Barriopedro, D., García-Herrera, R., Trigo, R., & Beguería, S. Examining the outstanding Euro-Mediterranean drought of 2021–2022 and its historical context. J. of Hydrol. 630, 130653 (2024). https://doi.org/10.1016/j.jhydrol.2024.130653.

[8] Allen, R. G. Crop evapotranspiration. FAO irrigation and drainage paper, 56, 60-64 (1998).

[9] Agnew, C. T. Using the SPI to identify drought. University College London, London, United Kingdom (2000).

[10] Gimeno-Sotelo, L., Fernández-Alvarez, J.C., Nieto, R. et al. The increasing influence of atmospheric moisture transport on hydrometeorological extremes in the Euromediterranean region with global warming. Commun Earth Environ 5, 604 (2024). https://doi.org/10.1038/s43247-024-01787-9.

[11] Stohl, A. & James, P. A. A Lagrangian analysis of the atmospheric branch of the global water cycle: Part II: Earth's river catchments ocean basins, and moisture transports between them. J. Hydrometeorol. 6, 961–984 (2005).

[12] Gimeno, L. et al. The residence time of water vapour in the atmosphere. Nat. Rev. Earth Environ. 2, 558-569 (2021).

[13] Gimeno, L. et al. Oceanic and Terrestrial Sources of Continental Precipitation. Rev. Geophysics 50, RG4003 (2012).

[14] Fernández-Alvarez, J. C., Pérez-Alarcón, A., Nieto, R., Gimeno, L. TROVA: TRansport Of water VApor. SoftwareX 20, 101228 (2022).

[15] Fernández-Alvarez, J. C., Pérez-Alarcón, A., Nieto, R., Gimeno, L. Version 1.1.1 - TROVA: TRansport Of water VApor. SoftwareX 30, 102135 (2025a). https://doi.org/10.1016/j.softx.2025.102135.

[16] Papritz, L.; Röthlisberger, M. A novel temperature anomaly source diagnostic: method and application to the 2021 heatwave in the Pacific Northwest. Geophys. Res. Lett., 50 (23), e2023GL105641 (2023).